# Chapter 14
# Simulating Quantum Dynamics in Classical Nanoscale Environments

**Gabriel Hanna and Alessandro Sergi**

**Abstract** In this chapter, we describe a mixed quantum-classical approach for simulating the dynamics of quantum mechanical phenomena occurring in nanoscale systems. This approach is based on the quantum-classical Liouville equation (QCLE), which prescribes the dynamics of a quantum subsystem coupled to a classical environment. We explain how the QCLE can be solved using a stochastic surface-hopping algorithm and how expectation values of observables can be computed. Schemes for reducing the number of trajectories required in these computations and for ensuring the continuous evolution of the quantum subsystem states along the trajectories are also outlined. To demonstrate the utility of these techniques, we describe two recent applications: vibrational energy transfer in an alpha-helical polypeptide and the field-driven dynamics of a plasmonic meta-molecule.

G. Hanna (✉)
Department of Chemistry, University of Alberta, Edmonton, AB, Canada
e-mail: gabriel.hanna@ualberta.ca

A. Sergi
Dipartimento di Scienze Matematiche e Informatiche, Scienze Fisiche e Scienze della Terra, Università degli Studi di Messina, Messina, Italy

Institute of Systems Science, Durban University of Technology, Durban, South Africa

Istituto Nazionale di Fisica Nucleare, Sez. di Catania, Catania, Italy
e-mail: asergi@unime.it

## 14.1  Introduction

Nanotechnologies have attracted the attention of many over the last several decades due to their versatility and advanced functionality. Optoelectronics [24, 88], molecular electronics [62] and quantum computing/information [8, 58, 59] are just a few prominent examples of fields that have benefitted tremendously from nanotechnologies. Nowadays, researchers are faced with the challenge of designing high-performance, efficient and environmentally friendly materials and devices. This challenge could translate into, for example, constructing devices that are capable of highly efficient transfer of energy [43, 57], charge [30, 54] or quantum information [58, 59] in complex nanostructures. To achieve such goals, however, one must gain a fundamental understanding of the dynamical processes involved and how these processes are influenced by their nanoscale environments. In this regard, molecular simulation has proven to be an indispensable tool for probing the structure and dynamics of nanoscale systems.

When the process under study is of a quantum nature and occurs in a complex, many-particle system such as a nanomaterial, a fully quantum approach to modelling the dynamics will be computationally intractable. In this case, an approximate treatment of the dynamics is required to gain insight into the process. Mixed quantum-classical dynamics methods, which treat a subsystem of interest quantum mechanically and the particles in its environment (or bath) in a classical-like fashion, can provide tremendous computational savings over fully quantum methods. For example, the subsystem could be a key proton/electron in a charge transfer reaction, a chromophore involved in a vibrational/electronic energy transfer process or an exciton in a light-harvesting system, while the environment could be a molecule, solvent or crystal.

The partitioning of a system into different sets of degrees of freedom (DOF) lies at the heart of the Born–Oppenheimer (BO) approximation, which assumes a time/energy scale separation between the motions of the nuclei and electrons. In quantum chemistry, the BO approximation greatly simplifies calculations of molecular energies and wave functions by enabling one to solve the electronic Schrödinger equation for a fixed configuration of the nuclei to obtain electronic energies and wave functions that depend on the nuclear configuration. By repeating this calculation for a sufficiently large number of nuclear configurations, one can then construct the potential energy surfaces (PESs) of the electronic subsystem. These PESs give rise to forces (known as Hellmann-Feynman forces) that act on the nuclei over the course of their dynamics. When the energy scale separation between the nuclei and electrons is sufficiently large, the nuclei will evolve subject to the forces obtained from the PES corresponding to the current state of the electrons (which will not change because the electrons will not have enough energy to hop to another PES). This is known as *adiabatic* dynamics. However, when their energy scales become comparable, the nuclei can evolve subject to the forces obtained from another PES (because the electrons may acquire enough energy from the nuclei to hop to another PES). This breakdown of the BO approximation is

**Fig. 14.1** A schematic representation of the ground and excited electronic PESs of a system. In adiabatic dynamics, the nuclei evolve on a single PES. However, in the vicinity of an avoided crossing, a nonadiabatic transition can occur, which causes the nuclei to evolve on another PES
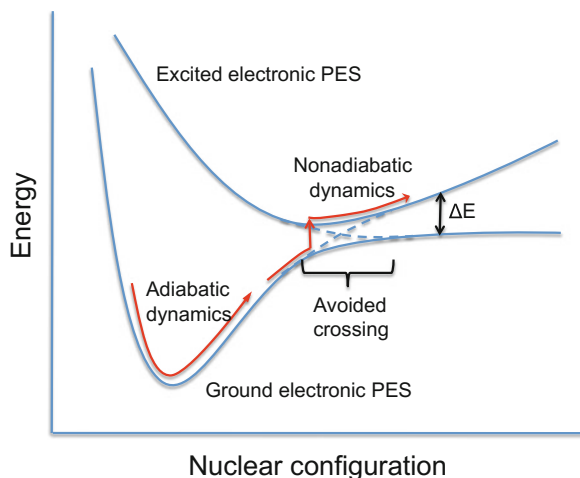


known as *nonadiabatic* dynamics. It typically occurs in the vicinity of an avoided crossing or conical intersection between PESs. (See Fig. 14.1 for an illustration of the aforementioned concepts.)

In general, adiabatic dynamics arises whenever one set of DOF changes slowly compared to another set, as in the case of nuclei and electrons in the BO approximation. If one is able to partition a system into a subsystem containing fast DOF of interest and an environment containing slow DOF, then the dynamics of the environmental DOF will be governed by a single PES corresponding to the state of the subsystem. However, when the time scales of motion of the subsystem and environmental DOF become comparable, motion on a single PES is no longer able to accurately capture the dynamics of the slower DOF. Many important processes in physics, chemistry and biology involve this nonadiabatic dynamics. Examples include intersystem crossings and internal conversions in photochemistry, electron transfer reactions in electrochemistry, ion–molecule reactions, reactions at metal surfaces, photo-induced dynamics of molecules adsorbed to semiconductor substrates (as in a photovoltaic cell) and photo-induced dynamics in quantum dots.

Due to the importance of nonadiabatic dynamics, a great deal of effort has been devoted to developing simulation methods over the years that take nonadiabatic effects into account. In particular, many mixed quantum-classical methods have been proposed for simulating nonadiabatic dynamics, which essentially differ in the way they couple the subsystem and bath DOF [1, 3, 25, 27, 33, 35, 39, 41, 48, 50, 61, 70, 74, 76, 81, 84, 85]. The two most widely used methods are mean-field (or Ehrenfest) and fewest switches surface-hopping (FSSH) dynamics [5–7, 10, 20, 29, 60, 67–69, 71, 75, 77, 86]. Mean-field dynamics is based on the assumption that the environmental motions are governed by a single effective PES, which is a weighted average over the adiabatic PESs of the subsystem. On the other hand, surface-hopping methods evolve the environmental DOF on a single adiabatic PES at any given time, with instantaneous hops to other PESs at times when the BO

approximation breaks down. However, mean-field and FSSH dynamics suffer from several drawbacks. Both methods do not correctly describe the "quantum back-reaction", i.e. the effect due to the subsystem-environment coupling, whereby a change in the environmental DOF modifies the subsystem Hamiltonian, which in turn modifies the forces governing the motion of the environmental DOF. Mean-field dynamics is not capable of capturing decoherence, while FSSH can do so after incorporating some ad hoc corrections [68, 71]. Both methods also struggle to satisfy detailed balance. Due to the incorrect nature of the energy transfer between the subsystem and environment, it is possible for the subsystem to approach unrealistically high temperatures in mean-field dynamics [55]; in such cases, one can employ quantum correction factors that modify the dynamics in such a way that detailed balance is enforced [4]. In FSSH, it is possible to satisfy detailed balance in certain limits if the so-called frustrated hops are allowed [64].

In this chapter, we focus on a mixed quantum-classical dynamics approach that is based on the quantum-classical Liouville equation (QCLE) [2, 22, 33, 89], which can be derived from the quantum Liouville equation by first taking its partial Wigner transform [87] over the bath DOF (leading to a description of the subsystem and bath DOF in terms of operators and phase space variables, respectively) and then truncating the resulting equation after first order in $\hbar$. The QCLE constitutes an ideal starting point [31, 32] for deriving mixed quantum-classical dynamics algorithms because (i) it can be rigorously derived from the more fundamental quantum Liouville equation based on a well-defined and physically reasonable approximation, and (ii) it yields the exact quantum dynamics for quantum subsystems that are bilinearly coupled to harmonic environments [45], which are frequently used models in chemical and condensed matter physics research. A large number of QCLE-based algorithms have been developed over the years [16–18, 23, 26–28, 34, 36, 37, 40, 41, 44, 46, 47, 49, 53, 63, 82, 83]. This chapter will deal with a particular algorithm known as sequential short-time propagation (SSTP) [23, 47], due to its favourable compromise between accuracy and ease of implementation. SSTP is a hybrid molecular dynamics/Monte Carlo algorithm, which relies on the so-called momentum jump approximation [23, 65] and solves the QCLE in terms of an ensemble of *surface-hopping* trajectories. However, a direct application of this algorithm has proven to be very challenging due to severe numerical instabilities that arise beyond short times when the subsystem-bath coupling strength is not very weak. In this case, the statistical weights associated with the Monte Carlo sampling of the nonadiabatic transitions (and that enter into the calculation of the observable) grow very rapidly in time, thereby necessitating very large numbers of trajectories to obtain converged expectation values. Transition filtering schemes [12, 13, 15, 23, 66, 79, 80], which impede the growth of these weights by filtering out the low-probability nonadiabatic transitions, have been shown to significantly alleviate the numerical instabilities. We will discuss one such scheme [12, 13] in this chapter.

In most mixed quantum-classical surface-hopping approaches (including the SSTP algorithm), one must evaluate the adiabatic states and nonadiabatic couplings between them at each time step of the simulation. In most cases, they are evaluated

numerically, which first entails a numerical diagonalization of the Hamiltonian matrix. However, the resulting eigenvectors are determined uniquely up to a sign, which leads to an arbitrariness in the signs of the nonadiabatic coupling vectors. These signs must be corrected by requiring that the eigenvectors change continuously from one point to the next along a trajectory in configuration space. However, the situation is further complicated when one is interested in computing time-dependent expectation values based on an ensemble of trajectories (which are typically initialized at different points in the configuration space). In this chapter, we outline a recently proposed method [14] for ensuring eigenvector sign continuity across an ensemble of trajectories in surface-hopping simulations.

To illustrate the utility of the aforementioned methods for simulating the dynamics of mixed quantum-classical systems, we present two applications. The first one demonstrates how transition filtering can be used to facilitate the calculation of amide I mode populations in a six-site model of an alpha-helical polypeptide, after a vibrational excitation at one end of the chain. The second one involves calculations of populations and coherences in a reduced model of a plasmonic metamolecule in an external field, using a generalized version of the SSTP algorithm for simulations of systems with time-dependent Hamiltonians.

The chapter is organized as follows. In Sect. 14.2, we present the QCLE, discuss how it can be solved via the SSTP algorithm, and explain how expectation values of observables can be computed. Recently proposed schemes for transition filtering and eigenvector sign correction are also outlined in this section. In Sect. 14.3, we present two recent applications of the aforementioned techniques to simulating vibrational energy transfer in an alpha-helical polypeptide and the field-driven dynamics of a plasmonic metamolecule. Our summary and future outlook are given in Sect. 14.4.

## 14.2 Mixed Quantum-Classical Liouville Dynamics

### 14.2.1 The Quantum-Classical Liouville Equation

We begin by considering a quantum subsystem, whose Hamiltonian operator is $\hat{H}_S$, embedded in a classical environment, whose Hamiltonian function is $H_B(Q, P) = \frac{P^2}{2M} + V(Q)$. The coordinates $(Q, P)$ denote the positions and momenta, respectively, of the atoms or molecular fragments (characterized by masses $M$ and interacting according to the potential energy function $V(Q)$) in the environment. The coupling between the quantum subsystem and classical environment is governed by the operator $\hat{H}_C(Q)$, which is also a function of the configuration of the environment. (In this chapter, we do not consider situations where the subsystem interacts with a magnetic field, such that the coupling Hamiltonian depends only on the configuration.) Hence, the Hamiltonian of the total system is given by

$$\hat{H}(Q, P) = \hat{H}_S + H_B(Q, P) + \hat{H}_C(Q) , \qquad (14.1)$$

**Fig. 14.2** A schematic
representation of the total
system and its components.
The Hamiltonian of the total
system is the sum of the
subsystem ($\hat{H}_S$), bath ($H_B$)
and coupling ($\hat{H}_C$)
Hamiltonians
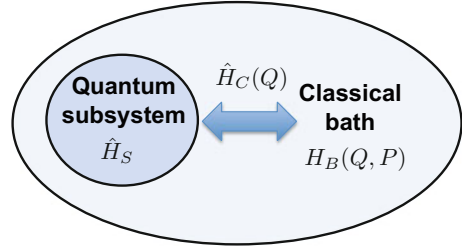


where $S$, $B$ and $C$ stand for subsystem, bath and coupling, respectively (see Fig. 14.2
for a schematic representation of the total system). The statistical and dynamical
properties of the hybrid quantum-classical system defined by the Hamiltonian in
Eq. (14.1) can be obtained in terms of the system's time-dependent density matrix
$\hat{\rho}(Q, P, t)$, which is also a function of the phase space coordinates $(Q, P)$. The
mixed quantum-classical dynamics of $\hat{\rho}(Q, P, t)$ is governed by the QCLE:

$$
\frac{\partial}{\partial t}\hat{\rho}(Q, P, t) = -\frac{i}{\hbar}\left[\hat{H}, \hat{\rho}(Q, P, t)\right] + \frac{1}{2}\left\{\hat{H}, \hat{\rho}(Q, P, t)\right\} - \frac{1}{2}\left\{\hat{\rho}(Q, P, t), \hat{H}\right\} ,
$$
$$(14.2)$$

where $[\cdot, \cdot]$ and $\{\cdot, \cdot\}$ denote the commutator and Poisson bracket, respectively. The
QCLE can either be postulated by requiring energy conservation (i.e. the antisym-
metry of the right-hand side guarantees that the time derivative of the Hamiltonian
$\hat{H}(Q, P)$ is identically zero) or derived from a fully quantum dynamical description
of the total system in the limit that the particles in the environment are much heavier
than those in the subsystem. This derivation first involves a representation of the
heavy coordinates in Wigner phase space, followed by a linearization of the resulting
equation in the smallness parameter $\mu = \sqrt{m/M}$, where $m$ is a characteristic
mass of the quantum DOF and $M$ is a characteristic mass of the classical DOF.
By coupling the dynamics of the quantum and classical DOF in this fashion, the
QCLE consistently describes the back-and-forth exchange of energy between the
quantum subsystem and classical environment.

Knowledge of $\hat{\rho}(Q, P, t)$ allows one to calculate the average of any observable
property of the system, which is represented in this formalism by a *microscopic* Her-
mitian operator that depends on the phase space point, i.e. $\hat{\chi}(Q, P) = \hat{\chi}^\dagger(Q, P)$.
Finally, the value of a *macroscopic* observable at time $t$ is given by

$$
\langle \hat{\chi}(t) \rangle = \text{Tr}' \int dQ dP \hat{\chi}(Q, P)\hat{\rho}(Q, P, t) ,
$$
$$(14.3)$$

where $\text{Tr}'$ denotes a partial trace over the quantum DOF. It is also possible to
evaluate the average in the Heisenberg picture,

$$\langle \hat{\chi}(t) \rangle = \text{Tr}' \int dQ dP \hat{\rho}(Q, P) \hat{\chi}(Q, P, t) \,, \qquad (14.4)$$

where the mixed quantum-classical equation of motion of $\hat{\chi}(Q, P, t)$ is given by

$$\frac{\partial}{\partial t} \hat{\chi}(Q, P, t) = \frac{i}{\hbar} \left[ \hat{H}, \hat{\chi}(Q, P, t) \right] - \frac{1}{2} \left\{ \hat{H}, \hat{\chi}(Q, P, t) \right\} + \frac{1}{2} \left\{ \hat{\chi}(Q, P, t), \hat{H} \right\} \,.$$
$$(14.5)$$

### 14.2.2   Representing the QCLE in the Adiabatic Basis

To arrive at a surface-hopping algorithm for solving the QCLE, one must first represent it in the adiabatic basis defined by the following eigenvalue problem (i.e. the time-independent Schrödinger equation):

$$\hat{H}_{\text{ad}}(Q)|\Phi_k(Q)\rangle = \epsilon_k|\Phi_k(Q)\rangle \,, \qquad (14.6)$$

where $\hat{H}_{\text{ad}}(Q) = \hat{H}_S + \hat{H}_C(Q) + V(Q)$ is the so-called adiabatic Hamiltonian operator, $|\Phi_k(Q)\rangle$ is the $k$th adiabatic basis state, and $\epsilon_k$ is the energy of that state. In this basis, the QCLE becomes [34]

$$\frac{\partial}{\partial t} \rho_{kk'}(Q, P, t) = -\sum_{jj'} \delta_{kj} \delta_{k'j'} \left( i\omega_{kk'} + iL_{kk'} \right) \rho_{jj'}(Q, P, t)$$

$$- \sum_{jj'} \mathcal{K}_{kk',jj'} \rho_{jj'}(Q, P, t) \,, \qquad (14.7)$$

where $\rho_{kk'}(Q, P, t) = \langle \Phi_k|\hat{\rho}(Q, P, t)|\Phi_{k'}\rangle$ are the density matrix elements, $\omega_{kk'} = [\epsilon_k(Q) - \epsilon_{k'}(Q)]/\hbar$ are the Bohr frequencies, $iL_{kk'}$ are the matrix elements of a classical-like Liouville operator

$$iL_{kk'} = \frac{P}{M} \frac{\partial}{\partial Q} + \frac{F_k(Q) + F_{k'}(Q)}{2} \frac{\partial}{\partial P} \,, \qquad (14.8)$$

with Hellmann-Feynman forces $F_k = -\partial \epsilon_k/\partial Q$, and $\mathcal{K}_{kk',jj'}$ are the matrix elements of a nonadiabatic transition super-operator

$$\mathcal{K}_{kk',jj'} = \delta_{k'j'} c_{kj}(Q, P) \left( 1 + \frac{1}{2} \frac{\hbar\omega_{kj}}{c_{kj}(Q, P)} d_{kj}(Q) \cdot \frac{\partial}{\partial P} \right)$$

$$+ \delta_{kj} c_{k'j'}^*(Q, P) \left( 1 + \frac{1}{2} \frac{\hbar\omega_{k'j'}}{c_{k'j'}^*(Q, P)} d_{k'j'}^*(Q) \cdot \frac{\partial}{\partial P} \right) \,, \qquad (14.9)$$

with $d_{kj} = \langle \Phi_k|\partial\Phi_j/\partial Q\rangle$ the nonadiabatic coupling vector and $c_{kj} = P/M \cdot d_{kj}$.

### 14.2.3    The Sequential Short-Time Propagation Algorithm

Now, we demonstrate how one can obtain a numerical algorithm for solving the QCLE in terms of a swarm of stochastic trajectories, where each trajectory is composed of piecewise deterministic segments interspersed with stochastic transitions of the quantum subsystem between different adiabatic states.

The sequential short-time propagation (SSTP) solution to Eq. (14.7) for $\rho_{kk'}(Q, P, t)$ is [47]

$$\rho_{kk'}(Q, P, t) = \sum_{(k_1 k_1')\ldots(k_N k_N')} \Big[ \prod_{j=1}^{N} (e^{-i\hat{\mathcal{L}}\Delta t_j})_{k_{j-1}k_{j-1}', k_j k_j'} \Big] \rho_{k_N k_N'}(Q, P), \tag{14.10}$$

where the time interval $t$ is divided into $N$ segments and $\Delta t_j = t_j - t_{j-1}$. In the limit that $\Delta t_j$ is sufficiently small, the propagator for segment $j$ may be approximated by

$$(e^{-i\hat{\mathcal{L}}\Delta t_j})_{k_{j-1}k_{j-1}', k_j k_j'} \approx \mathcal{W}_{k_{j-1}k_{j-1}'}(t_{j-1}, t_j) e^{-iL_{k_{j-1}k_{j-1}'}\Delta t_j}$$

$$\times \Big( \delta_{k_{j-1}k_j} \delta_{k_{j-1}'k_j'} - \Delta t \mathcal{K}_{k_{j-1}k_{j-1}', k_j k_j'} \Big), \tag{14.11}$$

where $\mathcal{W}_{k_{j-1}k_{j-1}'}(t_{j-1}, t_j) = e^{-i\omega_{k_{j-1}k_{j-1}'}\Delta t_j}$ is the phase factor associated with that segment. To simulate the action of $\mathcal{K}_{kk', jj'}$ on functions of the momenta, the momentum-jump approximation (MJA) [23, 65] is invoked, namely,

$$\left( 1 + \frac{\hbar\omega_{kj}}{2} \frac{d_{kj}}{c_{kj}} \cdot \frac{\partial}{\partial P} \right) f(P) = \left( 1 + \hbar\omega_{kj} \frac{\partial}{\partial(\bar{P} \cdot \bar{\hat{d}}_{kj})^2} \right) f(P)$$

$$\approx e^{\hbar\omega_{kj}\partial/\partial(\bar{P} \cdot \bar{\hat{d}}_{kj})^2} f(P)$$

$$= f(P + \Delta P), \tag{14.12}$$

where $\bar{P} = P/\sqrt{M}$, $\bar{\hat{d}}_{kj} = \bar{d}_{kj}/|\bar{d}_{kj}|$, $\bar{d}_{kj} = d_{kj}/\sqrt{M}$, and the momentum shift, $\Delta P$, is given by

$$\Delta P = \sqrt{M}\bar{\hat{d}}_{kj} \Big[ \mathrm{sgn}(\bar{P} \cdot \bar{\hat{d}}_{kj}) \sqrt{(\bar{P} \cdot \bar{\hat{d}}_{kj})^2 + \Delta\epsilon_{kj}} - (\bar{P} \cdot \bar{\hat{d}}_{kj}) \Big]. \tag{14.13}$$

(N.B.: $d_{kj}/\sqrt{M} = d_{kj}^T M^{-1/2}$, where $T$ stands for the transpose and $M^{-1/2}$ is a diagonal matrix containing the inverse square root of the masses.) According to Eq. (14.13), if $\Delta\epsilon_{kj} < 0$ (i.e. an upward transition from $k \to j$) and $(\bar{P} \cdot \bar{\hat{d}}_{kj})^2 < |\Delta\epsilon_{kj}|$ (i.e. there is insufficient kinetic energy from the bath momenta along $\bar{\hat{d}}_{kj}$ for the nonadiabatic transition to occur), then the argument of the square root is negative

leading to imaginary momentum changes. If this occurs, the nonadiabatic transition is forbidden, and the trajectory is continued adiabatically. It should be noted that the approximation made in the second line of Eq. (14.12) relies on $|\hbar\omega_{kj}d_{kj}c_{kj}^{-1}/2|$ being small. Also, the total energy of the system is conserved along a trajectory under the MJA.

The expectation value of $\hat{\chi}(Q, P, t)$ is given by

$$\langle\hat{\chi}(t)\rangle = \sum_{kk'}\int dQdP \chi_{k'k}(Q, P)\rho_{kk'}(Q, P, t)$$

$$= \sum_{(k_0k_0')\ldots(k_Nk_N')}\int dQdP \chi_{k_0'k_0}(Q, P)\Big[\prod_{j=1}^{N}(e^{-i\hat{\mathcal{L}}\Delta t_j})_{k_{j-1}k_{j-1}',k_jk_j'}\Big]\rho_{k_Nk_N'}(Q, P),$$

(14.14)

or, in the Heisenberg representation, by

$$\langle\hat{\chi}(t)\rangle = \sum_{kk'}\int dQdP \chi_{kk'}(Q, P, t)\rho_{k'k}(Q, P)$$

$$= \sum_{(k_0k_0')\ldots(k_Nk_N')}\int dQdP \rho_{k_0'k_0}(Q, P)\Big[\prod_{j=1}^{N}(e^{i\hat{\mathcal{L}}\Delta t_j})_{k_{j-1}k_{j-1}',k_jk_j'}\Big]\chi_{k_Nk_N'}(Q, P).$$

(14.15)

The SSTP algorithm evaluates Eq. (14.15) via a hybrid molecular dynamics (MD)/Monte Carlo (MC) approach, whereby the multidimensional sums over the state indices are evaluated using MC sampling, the initial conditions of the subsystem and bath are determined from $\rho_{k_0'k_0}(Q, P)$, and $\chi_{kk'}(Q, P, t)$ is propagated in time using MD simulation.

We now detail the steps of the SSTP algorithm for evaluating Eq. (14.15) by considering the evolution through a single time step (i.e. $N = 1$):

$$\langle\hat{\chi}(\Delta t)\rangle = \sum_{(k_0k_0')(k_1k_1')}\int dQdP \rho_{k_0'k_0}(Q, P)(e^{i\hat{\mathcal{L}}\Delta t_j})_{k_0k_0',k_1k_1'}\chi_{k_1k_1'}(Q, P).$$

$$= \sum_{(k_0k_0')(k_1k_1')}\int dQdP \rho_{k_0'k_0}(Q, P)\mathcal{W}_{k_0'k_0}(t_0, t_1)e^{iL_{k_0k_0'}\Delta t_1}$$

$$\times \Big(\delta_{k_0k_1}\delta_{k_0'k_1'} + \Delta t\mathcal{K}_{k_0k_0',k_1k_1'}\Big)\chi_{k_1k_1'}(Q, P). \qquad (14.16)$$

1. After specifying the initial density matrix, $\rho_{k_0'k_0}(Q, P)$, of the system, sample the initial conditions from $|\rho_{k_0'k_0}(Q, P)|$ using an appropriate scheme.
2. Propagate the bath DOF adiabatically on the adiabatic PES corresponding to the pair of indices $(k_0 k_0')$, i.e. $(\epsilon_{k_0} + \epsilon_{k_0'})/2$, for a time interval $\Delta t$, and calculate the phase factor $\mathcal{W}_{k_0'k_0}(0, \Delta t)$ for this interval.
3. According to Eq. (14.9) for $\mathcal{K}_{k_0 k_0' k_1 k_1'}$, determine stochastically whether or not a nonadiabatic transition $(k_0 k_0') \to (k_1 k_1')$ takes place. One way of sampling the nonadiabatic transitions involves first identifying which of the two terms in the expression for $\mathcal{K}_{k_0 k_0', k_1 k_1'}$ acts (viz. the first term changes the index $k_0 \to k_1$, while the second changes the index $k_0' \to k_1'$). This can be accomplished using MC by assigning a 50% probability to selecting each term. Once one of these terms has been selected, the actual transition is MC sampled with a probability

$$\mathcal{P}_{kj} = \frac{\Delta t |d_{kj} \cdot \frac{P}{M}|}{1 + \Delta t |d_{kj} \cdot \frac{P}{M}|}. \tag{14.17}$$

The probability of remaining in the same adiabatic state (i.e. no nonadiabatic transition) is therefore

$$\mathcal{Q}_{kj} = \frac{1}{1 + \Delta t |d_{kj} \cdot \frac{P}{M}|}, \tag{14.18}$$

satisfying $\mathcal{P}_{kj} + \mathcal{Q}_{kj} = 1$. If the transition is accepted, then the momenta are shifted according to Eqs. (14.12) and (14.13), and the value of the observable becomes

$$\chi_{k_1 k_1'}(\Delta t) = 2\mathcal{W}_{k_0 k_0'}(0, \Delta t) d_{kj} \cdot \frac{P_{\Delta t}}{M} \chi_{k_0 k_0'}(Q_{\Delta t}, P_{\Delta t} + \Delta P) \frac{1}{\mathcal{P}_{kj}}. \tag{14.19}$$

In the above equation, the factor of 2 is the MC weight associated with the sampling of the $k_0 \to k_1$ or $k_0' \to k_1'$ term in $\mathcal{K}_{k_0 k_0', k_1 k_1'}$ (which each occur with a probability of 50%), and $1/\mathcal{P}_{kj}$ is the MC weight associated with the sampling of the transition. On the other hand, if the transition is rejected, there is no momentum shift, and the value of the observable becomes

$$\chi_{k_1 k_1'}(\Delta t) = \mathcal{W}_{k_0 k_0'}(0, \Delta t) \chi_{k_0 k_0'}(Q_{\Delta t}, P_{\Delta t}) \frac{1}{\mathcal{Q}_{kj}}, \tag{14.20}$$

where $1/\mathcal{Q}_{kj}$ is the MC weight associated with no transition.
4. Repeat steps 2–3 until time $t$ to calculate $\chi_{k_N k_N'}(t)$.
5. Multiply $\chi_{k_N k_N'}(t)$ by the sign of the density matrix, and average the resulting value over the initial conditions to obtain $\langle \hat{\chi}(t) \rangle$.

### *14.2.4   Transition Filtering*

To obtain reliable expectation values beyond short times using the SSTP algorithm, experience has shown that one requires extremely large ensembles of trajectories. This is mainly due to the fact that the statistical weights associated with the MC sampling of the nonadiabatic transitions grow very rapidly in time, making it extremely difficult to obtain converged expectation values at longer times. More specifically, each trajectory acquires a statistical weight, $\prod_{j=1}^{N} \mathcal{W}_j$ (where $\mathcal{W}_j$ is the MC weight for time step $j$), which factors into the expectation value. In practice, these weights grow exponentially with time [12], thereby requiring an exponentially growing number of trajectories to converge expectation values at longer times. To slow down the growth of these weights and thereby reduce the number of trajectories required for convergence at longer times, observable cutting [23] and transition filtering [12, 13, 15, 66, 79, 80] schemes have been used, both separately and together, with varying degrees of success.

In observable cutting, one sets an upper bound on the magnitude of the weight at each time step of the simulation, thereby ensuring that the magnitude of the weight never becomes too large. Then, one computes the expectation value subject to this upper bound. To determine the value of the upper bound that will yield a satisfactory expectation value, one must repeat the calculation with increasingly larger values of the upper bound. Using this scheme, however, it is difficult to know if one has converged to the true result. In other words, if the upper bound is too small, the result may appear stable but may be inaccurate. Conversely, if the upper bound is too large, the result may be too noisy to be interpretable.

In contrast, transition filtering reduces the statistical noise by disallowing those nonadiabatic transitions that would lead to large statistical weights. In this subsection, we will outline the transition filtering approach proposed and implemented by Hanna et al. in Refs. [12, 13, 15]. In Refs. [12, 13], the scheme was laid out and applied to two relatively simple systems (viz. 2 quantum states coupled to 20 classical DOF and 3 quantum states coupled to 1 classical DOF), yielding substantial reductions in the numbers of trajectories required for convergence and smoother and more accurate results than those obtained with observable cutting. In Ref. [15], the scheme was applied to a model containing six quantum and six classical DOF, in order to investigate the feasibility and efficacy of the scheme for treating subsystems with larger numbers of states (as the number of trajectories scales with the number of states in the quantum subsystem). In this case, it was possible to obtain numerically stable results with more than one order of magnitude fewer trajectories than the number of trajectories used to generate the results without any filtering. This application will be discussed in more detail in Sect. 14.3.1.

We now outline the transition filtering scheme. To begin with, we define the following transition probability for the MC sampling of nonadiabatic transitions along an SSTP trajectory [12]

$$\Pi = \frac{\Delta t |A(Q, P)| w(\kappa_{\alpha\beta}, \Delta E_{\alpha\beta})}{1 + \Delta t |A(Q, P)| w(\kappa_{\alpha\beta}, \Delta E_{\alpha\beta})}, \qquad (14.21)$$

where $\Delta t$ is the time step and

$$w(\kappa_{\alpha\beta}, \Delta E_{\alpha\beta}) = \begin{cases} 1, & \text{if} |\Delta E_{\alpha\beta}| \le \kappa_{\alpha\beta}, \\ 0, & \text{otherwise.} \end{cases} \qquad (14.22)$$

As can be seen, this transition probability restricts nonadiabatic transitions between adiabatic PESs $\alpha$ and $\beta$ to occur when the magnitude of the energy gap between the surfaces is sufficiently small, i.e. less than a threshold value $\kappa_{\alpha\beta}$. The functional form of $A(Q, P)$ should be chosen in such a way to minimize the statistical noise in the expectation value. One form that has been shown to work relatively well is [12]

$$A(Q, P) = \frac{P}{M} \cdot d_{\alpha\beta} \frac{\Delta E_{\alpha\beta}^{\min}}{\Delta E_{\alpha\beta}}, \qquad (14.23)$$

where $\Delta E_{\alpha\beta}^{\min}$ is the smallest energy gap between the $\alpha$ and $\beta$ surfaces. In practice, $\Delta E_{\alpha\beta}^{\min}$ may be extracted from a $\Delta E_{\alpha\beta}$ histogram, generated by evolving the system adiabatically on its ground-state PES for a sufficiently long time. By filtering out nonadiabatic transitions with large $\Delta E_{\alpha\beta}$'s according to $w$ and placing $\Delta E_{\alpha\beta}$ in the denominator of $A(Q, P)$, one favours the high-probability transitions and thereby slows down the temporal growth of the statistical weights.

For an $n$-state quantum subsystem, one must specify the values of $n(n-1)/2$ $\Delta E_{\alpha\beta}^{\min}$'s and $\kappa_{\alpha\beta}$'s (because there are $n(n-1)/2$ possible $\alpha \leftrightarrow \beta$ nonadiabatic transitions). The $\Delta E_{\alpha\beta}^{\min}$ values may be obtained as explained in the previous paragraph, while sensible initial trial values for the $\kappa_{\alpha\beta}$'s are the mean values of the $\Delta E_{\alpha\beta}$'s. Using the SSTP algorithm, one then computes a time-dependent expectation value out to some time $t$, using a reasonably large number of trajectories. If the result is noisy, one may converge the expectation value according to the following steps:

1. Reduce the value of $\kappa_{1n}$ (relative to its previous value) to filter the $1 \leftrightarrow n$ transitions and recompute the expectation value out to time $t$.
2. If the result is noisy, then further reduce the values of $\kappa_{\alpha\beta}$ to filter the transitions between states for which $|\alpha - \beta| = n - 2$ (e.g. in the $n = 4$ case, the $1 \leftrightarrow 3$ and $2 \leftrightarrow 4$ transitions) and recompute the expectation value out to time $t$.
3. If $n > 3$, then repeat the previous step for the transitions with $|\alpha - \beta| = n - k$ (where $k = 3 \ldots n - 1$).
4. If the result is noisy, repeat steps 1 to 3.

## 14.2.5  Eigenvector Sign Correction

In nonadiabatic dynamics methods such as the SSTP algorithm, the adiabatic states and nonadiabatic couplings between them must be evaluated on-the-fly. Typically, they are evaluated numerically, which first involves a numerical diagonalization of the Hamiltonian matrix (represented in a convenient basis). The diagonalization results in eigenvectors that are uniquely determined up to a sign, which leads to arbitrary signs of the nonadiabatic coupling vectors. The signs may be corrected by requiring that the eigenvectors change continuously from one time step to the next. However, when a system is in the vicinity of an avoided crossing or conical intersection between two PESs, it becomes more complicated to correctly distinguish between physical and unphysical sign changes in the eigenvectors. Previously, Errea et al. proposed a procedure for correcting the sign of an electronic state, which involves tracking the sign of the overlap between the state evaluated at neighbouring points in a grid of nuclear positions [19]. This procedure also accounts for situations in which the system is in the vicinity of an avoided crossing or conical intersections.

The procedure put forward in Ref. [19] focuses on ensuring the continuous evolution of eigenvectors and nonadiabatic coupling vectors along a single trajectory in configuration space. However, when computing time-dependent expectation values based on an ensemble of trajectories (which are typically initialized at different points in configuration space), one is faced with the issue of how to ensure eigenvector sign continuity within the ensemble. In Ref. [14], building upon elements of Errea et al.'s method, Hanna et al. proposed a simple procedure that accomplishes this within the context of mixed quantum-classical surface-hopping dynamics simulations. The utility of this procedure was demonstrated by calculating both adiabatic state populations in a reduced model of a condensed phase proton-coupled electron transfer reaction and subsystem state populations in an excitonic model of an alpha-helical chain undergoing vibrational energy transport, using the SSTP algorithm. More specifically, the results showed that ensuring eigenvector sign continuity across the ensemble leads to minor (but significant) improvements in the accuracy of expectation values in some cases and to drastic improvements in other cases.

We now outline the procedure proposed in Ref. [14]. To properly evaluate the expression for a time-dependent expectation value in Eq. (14.15), the sign continuity of the eigenvectors must be preserved across all of the points in the configurational space (of the classical DOF) visited by an ensemble of trajectories, as opposed to the points within a single trajectory. This may be accomplished by first sampling the initial conditions of the classical DOF for the first microcanonical (i.e. NVE) trajectory from a canonical (i.e. NVT) trajectory, in which the eigenvector signs are tracked and corrected at each time step according to the following steps:

1. Compute $O_{\alpha\alpha}(t) = \langle \alpha; Q_t | \alpha; Q_{t-\Delta t} \rangle$ (i.e. the overlap of eigenvector $\alpha$ with eigenvector $\alpha$ of the previous time step) for each $\alpha$. When the classical configuration $Q_{t-\Delta t}$ is not close to an avoided crossing or conical intersection

and the time step is sufficiently small, the eigenvectors are not expected to rotate by much. In this case, the $O_{\alpha\alpha}$'s will be close to 1 (assuming that the eigenvectors are normalized). However, if an eigenvector undergoes an arbitrary sign flip, then the $O_{\alpha\alpha}$'s will be close to -1. In contrast, when $Q_{t-\Delta t}$ is close to an avoided crossing or conical intersection, the eigenvectors may vary rapidly, leading to $O_{\alpha\alpha}$'s that are substantially lower than 1 and possibly even negative. In this case, if an eigenvector undergoes an arbitrary sign flip, then $O_{\alpha\alpha}$ could lie in the interval $-\delta < O_{\alpha\alpha} < \delta$, where $|\delta|$ is substantially lower than 1 (e.g. 0.7 or lower).

2. Determine the value of $m_t(\alpha)$ for all $\alpha$'s, according to

$$m_t(\alpha) = \begin{cases} 0 & \text{if } |O_{\alpha\alpha}(t) - 1| < \epsilon \\ 1 & \text{if } |O_{\alpha\alpha}(t) + 1| < \epsilon \\ 2 & \text{otherwise} \end{cases} \qquad (14.24)$$

where $\epsilon$ is a threshold parameter (with $0 < \epsilon < 1$) that depends on the size of the time step, $\Delta t$, and the details of the PESs. The $m_t(\alpha) = 0$ and 1 cases would typically arise when $Q_{t-\Delta t}$ is not in the vicinity of an avoided crossing or conical intersection and the eigenvector undergoes a physical rotation and unphysical sign flip, respectively. The $m_t(\alpha) = 2$ case would typically arise when $Q_{t-\Delta t}$ is in the vicinity of an avoided crossing or conical intersection. In this case, one must return the system to the end of the previous time step, divide the current time step in half, and evolve the system with the reduced time step. This process is repeated until $m_t(\alpha)$ becomes either 0 or 1. A sensible choice of $\epsilon$ (in combination with a sufficiently small $\Delta t$) should yield $m_t(\alpha) = 0, 1$ most of the time (in order to minimize the number of time steps needed).

3. Correct the signs of all eigenvectors according to

$$|\alpha; Q_t\rangle^c = (-1)^{m_t(\alpha)}|\alpha; Q_t\rangle, \qquad (14.25)$$

i.e. if $m_t(\alpha) = 0$, then the sign is not changed, and if $m_t(\alpha) = 1$, then the sign is flipped to ensure the continuous evolution of the eigenvector.

At the end of this NVT dynamics phase, the eigenvectors are stored in memory (i) to continue the sign tracking and correction during the first NVE trajectory in the ensemble and (ii) to continue the sign tracking and correction during the second NVT dynamics phase preceding the second NVE trajectory. This procedure is repeated for the remaining trajectories in the ensemble (see Fig. 14.3 for an illustration of this procedure). In this way, the basis coefficients in $|\alpha; Q\rangle = \sum_i c_i^\alpha(Q)|\phi_i\rangle$ (where $\{|\phi_i\rangle\}$ is a basis set of choice), which may enter explicitly into the sampling of $\rho_{\alpha'\alpha}(Q, P)$ and into the dynamics of $\chi_{\alpha\alpha'}(Q, P, t)$, will evolve continuously throughout the configurational space.

For systems that do not spend a significant amount of time in the vicinity of an avoided crossing or conical intersection, one can reduce the computational time

**Fig. 14.3** A pictorial depiction of the procedure for ensuring sign continuity within an ensemble of trajectories
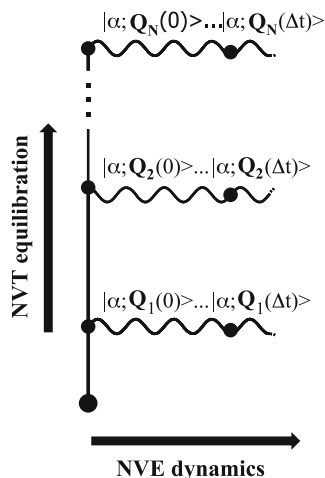


**Fig. 14.4** Histogram of all eigenvector overlap values, $O_{\alpha\alpha}$, for the PCET model considered in Ref. [14]. The inset portrays a zoomed in portion of the histogram
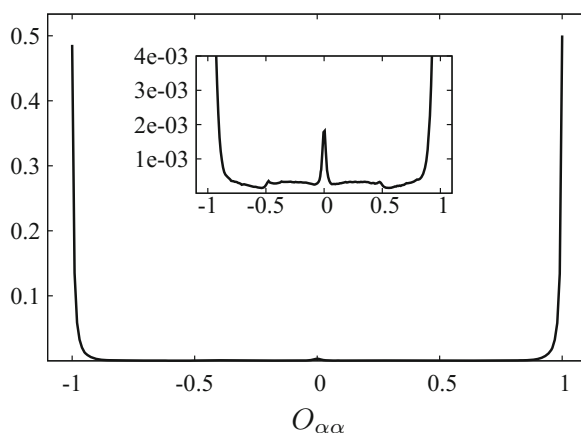


associated with implementing the $m_t(\alpha) = 2$ case by neglecting it altogether, i.e. one does not change the sign of the eigenvector (based on the assumption that any sign change is physical in this region of the configurational space). In such situations, one must choose the value of $\epsilon$ with great care. If $\epsilon$ is too large, then one could erroneously change the eigenvector signs and, in turn, distort the results. We now discuss a way of choosing appropriate $\epsilon$ values for a given system and time step size (in general, the optimal value of $\epsilon$ will depend on these factors). To determine which value or range of values would be appropriate, it is instructive to first generate a histogram of the $O_{\alpha\alpha}$ values. In Fig. 14.4, we present the histogram of $O_{\alpha\alpha}$ values for the proton-coupled electron transfer (PCET) model considered in Ref. [14], which was calculated based on a sufficiently large ensemble of "sign-uncorrected" trajectories. As can be seen, the most probable values of $O_{\alpha\alpha}$ occur in the ranges $-1 < O_{\alpha\alpha} < -0.9$ and $0.9 < O_{\alpha\alpha} < 1$, with the remaining $O_{\alpha\alpha}$ values having very low probabilities. Zooming in on the region at low ordinate values (see inset of

Fig. 14.4), one sees continuous decays starting from $O_{\alpha\alpha} = \pm 1$, followed by two blips centred at $O_{\alpha\alpha} \approx \pm 0.5$, and a peak centred at $O_{\alpha\alpha} = 0$ (which is presumably due to character switches in the eigenstates after a nonadiabatic transition). The discontinuities at $O_{\alpha\alpha} \approx \pm 0.5$ are suggestive of the onset of eigenvector rotations near an avoided crossing or conical intersection and thereby point to an optimal $\epsilon$ value that is slightly less than $\approx 0.5$.

To validate the accuracy of the expectation values calculated using the stream-lined version of the eigenvector sign correction procedure, one could repeat the calculation with a reduced time step and compare the results to those obtained with the larger time step. (For the system considered in Ref. [14], it was found that the percentage of the total time that the $m_t(\alpha) = 2$ case arises for a particular choice of $\epsilon$ decreases by about two orders of magnitude when the time step is decreased by at least a factor of ten.) If there is no significant change in the results, then the streamlined method is justified.

Finally, to speed up the generation of the ensemble of trajectories, one can split up the work onto many computer processors. As a result, however, one can no longer easily ensure eigenvector sign continuity across the entire ensemble, but only within the sub-ensemble of trajectories generated on a given processor. In Ref. [14], the authors confirmed that the final expectation values were not adversely affected by the parallelization by checking what happens after randomizing the initial eigenvector signs every $n$ trajectories on each processor. This check revealed that for the system considered, one must run at least $\approx 400$ trajectories per processor to recover the fully sign-corrected results.

## 14.3 Applications

### 14.3.1 Vibrational Energy Transfer in an Alpha-Helical Polypeptide

We now present an application in which the utility of the previously discussed transition filtering scheme is demonstrated for simulating vibrational energy transfer in a six-state model of an alpha-helical polypeptide [15]. In this case, the vibrational energy transfer is monitored by computing the time-dependent amide I mode populations, following a vibrational excitation at one end of the polypeptide.

The aforementioned model, portrayed in Fig. 14.5, involves a one-dimensional chain of hydrogen-bonded (H-bonded) peptide groups, constituting one of the three peptide chains in an alpha-helical polypeptide. Adopting a mixed quantum-classical description, the high-frequency amide I modes are treated quantum mechanically, while the low-frequency H-bond displacement coordinates to which the amide I modes are coupled are treated classically. The Hamiltonian of this system is given by

$$H = H_0 |0\rangle\langle 0| + \sum_{m,n} H_{mn} |\phi_m\rangle\langle\phi_n|, \tag{14.26}$$
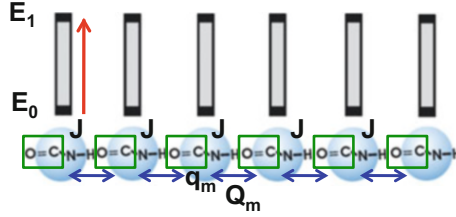
**Fig. 14.5** One-dimensional chain model of H-bonded peptide groups (blue spheres) in an alpha-helical polypeptide. The position of the $m$th amide I mode (green rectangles) is denoted by $q_m$, while the longitudinal displacement of the $m$th unit (blue double-sided arrows) is denoted by $Q_m$. Initially, the first amide I mode in the chain is vibrationally excited (as indicated by the red arrow) with energy $E_1$, and the remainder of the amide I modes are in their ground states with energies $E_0$

where $|\phi_m\rangle = |\chi_{m1}\rangle \prod_{n \neq m} |\chi_{n0}\rangle$ is the $m$th singly excited state and $|0\rangle = \prod_m |\chi_{m0}\rangle$ is the ground state of a chain of amide I modes. (N.B.: $|\chi_{m0}\rangle$ and $|\chi_{m1}\rangle$ denote the ground and first excited states, respectively, of the $m$th amide I mode). The ground-state matrix element is given by $H_0 = T + \mathcal{E}_0(Q)$, where $T = \Sigma_i \frac{P_i^2}{2M}$ is the kinetic energy associated with the motion of the H-bond lattice displacements and the potential energy has the following form:

$$\mathcal{E}_0(Q) = \sum_m \left[ E_{m0} + (1 - \delta_{m,1}) \frac{W}{2} (Q_m - Q_{m-1})^2 + w_{m0}(Q) \right]. \qquad (14.27)$$

The excited state matrix elements are given by

$$
\begin{aligned}
H_{mn} = &\ \delta_{m,n} \left[ H_0 + E_{m1} - E_{m0} + w_{m1}(Q) - w_{m0}(Q) \right] \\
&- J \left[ \delta_{m-1,n} \langle \phi_m | q_m q_{m-1} | \phi_{m-1} \rangle \right. \\
&\left. + \delta_{m,n-1} \langle \phi_n | q_n q_{n-1} | \phi_{n-1} \rangle \right],
\end{aligned} \qquad (14.28)
$$

where $\delta_{i,j}$ is the Kronecker delta function, $J$ is the parameter governing the strength of the transition dipole moment coupling between neighbouring amide I modes, $W$ is the force constant governing the motion of the H-bond lattice displacements, $E_{m1} - E_{m0}$ is the energy gap between the ground and first excited states of the $m$th amide I mode, $q_m$ is the position of the $m$th amide I mode, and $Q = \{Q_m\}$ corresponds to the set of H-bond lengths. The term $w_{mv}(Q)$, which describes the coupling between the H-bond displacements and the amide I modes, is given by

$$w_{mv}(Q) = (1 - \delta_{m,1}) \frac{\chi}{2} (Q_m - Q_{m-1}) \langle \chi_{mv} | q_m^2 | \chi_{mv} \rangle, \qquad (14.29)$$

where $\chi$ is the coupling strength. The values of the various matrix elements of $q_m$ and $q_m^2$ are taken from Table 2 in Ref. [73], while the values of the parameters

$E_{m1} - E_{m0}$, $J$, $W$, $\chi$ and $M$ are taken from Table 1 in Ref. [73] and are given by $1660\,\mathrm{cm}^{-1}$, $7.8\,\mathrm{cm}^{-1}$, $13\,\mathrm{N/m}$, $62\,\mathrm{pN}$ and $87\,m_p$, respectively.

The quantum subsystem of amide I modes and classical environment of H-bond lattice displacements are uncorrelated initially, which yields the following factorized initial density matrix:

$$\hat{\rho}(0) = \hat{\rho}_q(0)\,\rho_e(Q, P), \qquad (14.30)$$

where $\hat{\rho}_q(0)$ and $\rho_e(Q, P)$ correspond to the initial densities of the quantum subsystem and classical environment, respectively. Following a vibrational excitation of the first amide I mode in the chain, the initial density matrix of the quantum subsystem, represented in the subsystem basis of singly excited states, is given by

$$\hat{\rho}_q(0) = \begin{pmatrix} 1 & 0 & \cdots & 0 \\ 0 & 0 & \cdots & 0 \\ \vdots & \vdots & \ddots & 0 \\ 0 & 0 & \cdots & 0 \end{pmatrix}. \qquad (14.31)$$

The positions and momenta of the classical oscillators are initialized by first treating them as a collection of uncoupled harmonic oscillators at thermal equilibrium at 300 K, whose equilibrium Wigner distribution $\rho_e(Q, P)$ can be well approximated by

$$\rho_e(Q, P) \approx \frac{1}{Z} \prod_{j=1}^{M} \exp\left[ -\beta \left\{ \frac{P_j^2}{2} + \frac{1}{2} W^2 Q_j^2 \right\} \right], \qquad (14.32)$$

where $M$ is the number of oscillators and $Z = \int dQ\,dP \exp\left[ -\frac{\beta}{2} \sum_j (P_j^2 + W^2 Q_j^2) \right]$ is the partition function. The correct thermal equilibrium distribution at 300 K (in the absence of any amide I excitation) is then achieved by equilibrating the coupled harmonic oscillators for 2 ps using the ground-state potential found in Eq. (14.27) with a Nosé-Hoover thermostat and a time step of 0.25 fs. (In Ref. [21], the ergodicity of the Nosé-Hoover thermostat was confirmed by comparing the results to those generated with a Nosé-Hoover chain thermostat.) The initial state of the quantum oscillators is sampled by first transforming $\hat{\rho}_q(0)$ to the adiabatic basis (see details of the transformation and sampling in Appendix A of Ref. [21]). Following the classical equilibration and sampling of the initial quantum state, a 50-fs microcanonical SSTP trajectory is generated using a time step of 1 fs. The arbitrary sign flips in the eigenvectors upon numerical diagonalization of the Hamiltonian matrix are corrected at each time step using the procedure described in Sect. 14.2.5.

Before presenting the results for the time-dependent populations of the amide I modes, one must describe how the optimal values of $\Delta E_{\alpha\beta}^{\min}$ and $\kappa_{\alpha\beta}$ are determined (see Sect. 14.2.4 for the definitions of these quantities). Because the basis set

**Fig. 14.6** Histograms of $|\Delta E_{\alpha\beta}|$ values (in units of $10^{-22}$ J) for all 15 possible energy gaps between the adiabatic states. The mean value of each histogram is denoted by a vertical arrow. Each colour corresponds to energy gaps with the same value of $|\alpha - \beta|$
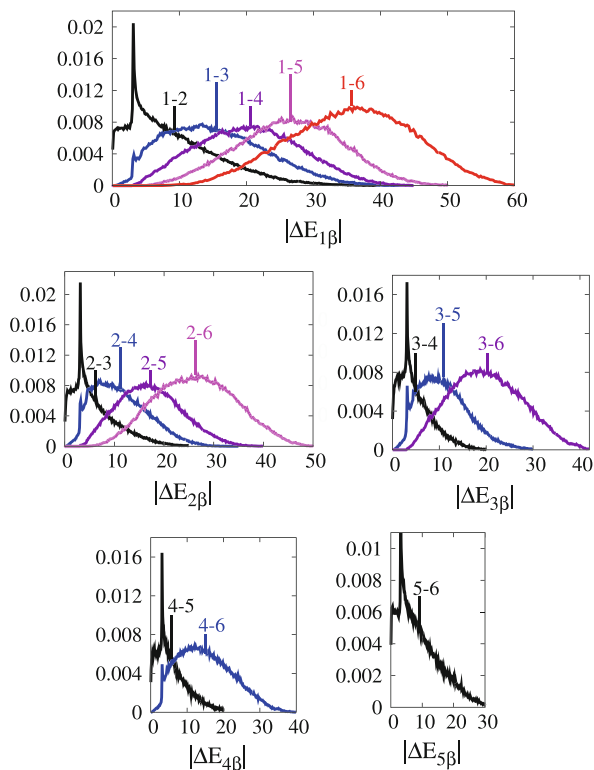
contains six singly excited states (one per amide I mode), the number of adiabatic states involved in the dynamics is $n = 6$, and, therefore, one has to determine 15 $\Delta E_{\alpha\beta}^{\min}$ values and 15 $\kappa_{\alpha\beta}$ values. To accomplish this, the system is evolved adiabatically on its ground-state PES for a sufficiently long time (i.e. to explore the important regions of the configuration space of the classical DOF), and 15 $|\Delta E_{\alpha\beta}|$ histograms are generated based on the $\Delta E_{\alpha\beta}$ values calculated at each time step (see histograms in Fig. 14.6). The first, second and third columns of Table 14.1 show the $\Delta E_{\alpha\beta}^{\min}$ values corresponding to the smallest $\Delta E_{\alpha\beta}$ values with a non-zero probability density in the histograms, the mean values of each $|\Delta E_{\alpha\beta}|$ histogram and the optimal $\kappa_{\alpha\beta}$ values used to generate the results, respectively. It should be noted that the $|\alpha - \beta| = 1$ transitions (whose $|\Delta E_{\alpha\beta}|$ histograms have substantial probability densities at lower $|\Delta E_{\alpha\beta}|$ values) are not filtered in an effort to minimize the errors introduced by filtering out transitions.

Figure 14.7 shows the time-dependent populations of the amide I modes out to 50 fs, generated using the transition filtering scheme, $10^9$ trajectories and a time step of 1 fs. Comparing these results to the unfiltered ones [14] generated using $5 \times 10^{10}$ trajectories, one sees that it is possible to obtain smoother and comparably accurate results with more than an order of magnitude fewer trajectories when transition filtering is used.

**Table 14.1** The values of the transition filtering parameters used in the simulations. All values are in units of $10^{-22}$ J

| $\alpha \leftrightarrow \beta$ | $\Delta E_{\alpha\beta}^{\min}$ | $\overline{\Delta E}_{\alpha\beta}$ | $\kappa_{\alpha\beta}$ |
|---|---|---|---|
| $1 \leftrightarrow 2$ | 0.00182 | 9.3 | – |
| $1 \leftrightarrow 3$ | 0.255 | 15.53 | 8 |
| $1 \leftrightarrow 4$ | 3.117 | 20.57 | 12 |
| $1 \leftrightarrow 5$ | 5.103 | 26.55 | 20 |
| $1 \leftrightarrow 6$ | 6.327 | 35.72 | 23 |
| $2 \leftrightarrow 3$ | 0.00035 | 6.19 | – |
| $2 \leftrightarrow 4$ | 0.229 | 11.27 | 8 |
| $2 \leftrightarrow 5$ | 3.117 | 17.27 | 12 |
| $2 \leftrightarrow 6$ | 4.826 | 26.42 | 20 |
| $3 \leftrightarrow 4$ | 0.0004 | 5.02 | – |
| $3 \leftrightarrow 5$ | 0.181 | 11.01 | 8 |
| $3 \leftrightarrow 6$ | 3.119 | 20.19 | 12 |
| $4 \leftrightarrow 5$ | 0.000577 | 5.76 | – |
| $4 \leftrightarrow 6$ | 0.234 | 15.15 | 8 |
| $5 \leftrightarrow 6$ | 0.00119 | 8.98 | – |
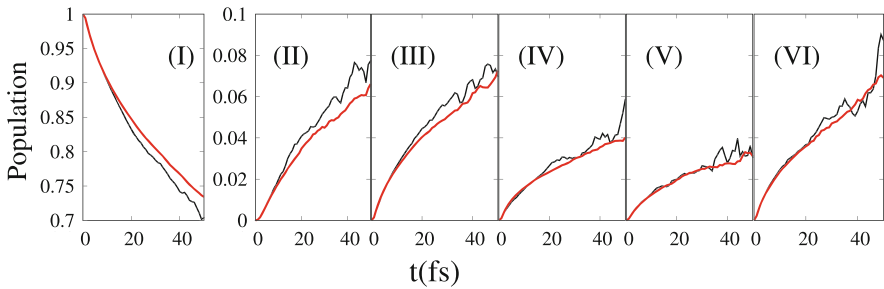


**Fig. 14.7** Comparison of the time-dependent populations of the six amide I modes, generated with the transition filtering scheme (red lines) and without any filter (black lines). (The unfiltered results are taken from Ref. [14])

### 14.3.2 Field-Driven Dynamics of a Plasmonic Metamolecule

We next present an application in which the SSTP algorithm is generalized for simulating the dynamics of a metamolecule subjected to a time-dependent driving field [78]. In this case, because the Hamiltonian is time-dependent, a time-dependent basis is used. Metamolecules are important in the field of quantum plasmonics [9, 11, 72, 90], which studies the interactions of surface plasmons with quantum emitters (a metamolecule collectively refers to the surface plasmon and quantum emitter). At the nanometre scale, metamolecules can operate at optical frequencies [38, 42, 52, 56]. A typical example of such a metamolecule is a quantum dot coupled to a surface plasmon in a metal nanoparticle [51].

A metamolecule can be modelled by a two-level system, representing the quantum dot, coupled to a resonant mode, representing the surface plasmon in
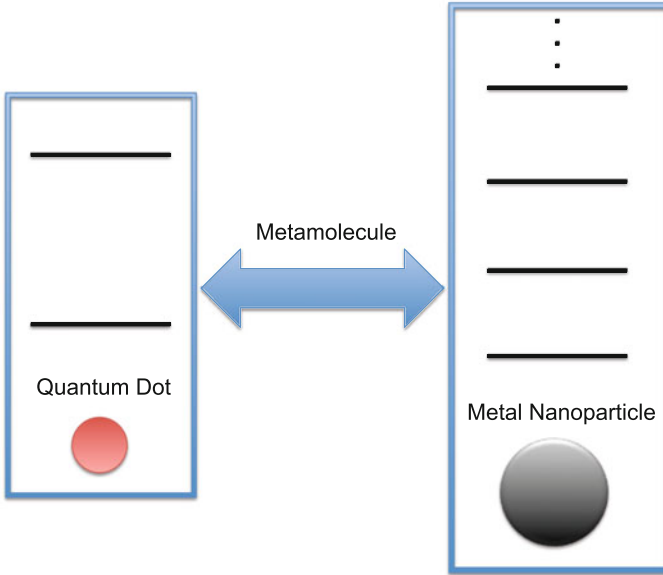
**Fig. 14.8** A schematic illustration of a model metamolecule. The metamolecule is composed of a quantum dot, represented by a two-level system, coupled to a surface plasmon in a metal nanoparticle and represented by a quantum harmonic oscillator (with a manifold of equispaced energy levels)

the metal nanoparticle (see Fig. 14.8 for a schematic illustration) [72]. In addition, the effect of a time-dependent driving field on the dynamics of the metamolecule can be considered. In this section, we present a study in which the two-level system is treated quantum mechanically and the resonant mode and driving field are treated classically. The time-dependent Hamiltonian of this mixed quantum-classical system, written in terms of adimensional quantities (whose definitions are given in the Appendix), is given by

$$\hat{H}(t) = -\frac{\Omega}{2}\hat{\sigma}_z + \frac{P^2}{2} + \frac{1}{2}\omega^2 Q^2 - cQ\hat{\sigma}_x + g\cos(\omega_d t)\hat{\sigma}_x , \qquad (14.33)$$

where $\Omega$ is the frequency associated with the two-level system, $\omega$ is the frequency associated with the resonant mode, $c$ is a coupling constant, $g$ denotes the subsystem-field coupling strength, $\omega_d$ is the driving frequency, and $\hat{\sigma}_{x/z}$ denote the Pauli matrices. The composite system is initialized in the factorized state $\hat{\rho}(Q, P) = \hat{\rho}_S \rho_B(Q, P)$, where the density matrix of the subsystem (i.e. the two-level quantum dot), expressed in the subsystem basis, is given by

$$\hat{\rho}_S = \begin{pmatrix} 0 & 0 \\ 0 & 1 \end{pmatrix}, \qquad (14.34)$$

and $\rho_B(Q, P)$, the Wigner distribution function of the bath (i.e. the resonant harmonic mode), is given by

$$\rho_B(Q, P) = \frac{\tanh(\beta\omega/2)}{\pi} \exp\left[-\frac{2\tanh(\beta\omega/2)}{\omega}\left(\frac{P^2}{2} + \frac{\omega^2 Q^2}{2}\right)\right]. \quad (14.35)$$

To simulate the quantum-classical Liouville dynamics of the Hamiltonian in Eq. (14.33), a generalization of the SSTP algorithm to time-dependent Hamiltonians is needed. To this end, one can introduce a time-dependent basis in terms of the eigenstates of $\hat{h}(Q, t) = \hat{H}(Q, P, t) - P^2/2M$ (defined by $\hat{h}(Q, t)|\alpha; Q, t\rangle = E_\alpha(Q, t)|\alpha; Q, t\rangle$, where $|\alpha; Q, t\rangle$ and $E_\alpha(Q, t)$ are the $\alpha$th eigenstate and eigenvalue, respectively). In this basis, the evolution of an observable $\chi$ takes the form

$$\chi_{\alpha\alpha'}(Q, P, t) = \mathcal{T}\left\{\sum_{\beta\beta'}\left(e^{i\int_{t_0}^t d\tau \mathcal{L}^t(\tau)}\right)_{\alpha\alpha', \beta\beta'}\right\} \chi_{\beta\beta'}(Q, P, t_0), \quad (14.36)$$

where $t_0$ is the initial time, $\mathcal{T}$ is the time-ordering operator and

$$i\mathcal{L}_{\alpha\alpha', \beta\beta'}^t(t) = i\tilde{\mathcal{L}}_{\alpha\alpha', \beta\beta'}(t) + \mathcal{K}_{\alpha\alpha', \beta\beta'}^t(t). \quad (14.37)$$

In the above equation, the operator $\mathcal{K}^t$ is responsible for the nonadiabatic transitions in the subsystem due to the interaction with the external field, and its matrix elements are given by

$$\mathcal{K}_{\alpha\alpha', \beta\beta'}^t = \langle\dot{\alpha}|\beta\rangle\delta_{\alpha'\beta'} + \langle\beta|\dot{\alpha}'\rangle\delta_{\alpha\beta}, \quad (14.38)$$

where the dot denotes a time derivative. The matrix elements of the operator $i\tilde{\mathcal{L}}$ have a similar form to those implied in Eq. (14.7) and are given by

$$i\tilde{\mathcal{L}}_{\alpha\alpha', \beta\beta'}(t) = i\tilde{\mathcal{L}}_{\alpha\alpha'}^0(t)\delta_{\alpha\beta}\delta_{\alpha'\beta'} + \tilde{\mathcal{K}}_{\alpha\alpha', \beta\beta'}(t), \quad (14.39)$$

where $i\tilde{\mathcal{L}}_{\alpha\alpha'}^0(t) = i\tilde{\omega}_{\alpha\alpha'}(t) + i\tilde{L}_{\alpha\alpha'}(t)$, with the Bohr frequency $\tilde{\omega}_{\alpha\alpha'}(Q, t) = [E_\alpha(Q, t) - E_{\alpha'}(Q, t)]/\hbar$ and the classical-like Liouville operator $i\tilde{L}_{\alpha\alpha'} = (P/M)\cdot(\partial/\partial Q) + (1/2)[\tilde{F}_W^\alpha(t) + \tilde{F}_W^{\alpha'}(t)]\cdot\partial/\partial P$ ($\tilde{F}_W^\alpha(Q, t)$, is the time-dependent Hellman-Feynman force derived from the adiabatic energy surface $E_\alpha(Q, t)$); the operator $\tilde{\mathcal{K}}$ is responsible for nonadiabatic transitions in the subsystem due to the interaction with the bath and its matrix elements are given by

$$\tilde{\mathcal{K}}_{\alpha\alpha', \beta\beta'}(t) = \tilde{\mathcal{T}}_{\alpha\to\beta}(t)\delta_{\alpha'\beta'} + \tilde{\mathcal{T}}_{\alpha'\to\beta'}^*(t)\delta_{\alpha\beta}, \quad (14.40)$$

where

$$\tilde{\mathcal{T}}_{\alpha\to\beta}(t) = \frac{P}{M}\cdot d_{\alpha\beta}(Q, t)\left(1 + \frac{1}{2}\frac{\Delta E_{\alpha\beta}(t)d_{\alpha\beta}(Q, t)}{\frac{P}{M}\cdot d_{\alpha\beta}(Q, t)}\frac{\partial}{\partial P}\right), \quad (14.41)$$

$$\tilde{\mathcal{T}}^*_{\alpha' \to \beta'}(t) = \frac{P}{M} \cdot d^*_{\alpha' \beta'}(Q, t) \left( 1 + \frac{1}{2} \frac{\Delta E_{\alpha' \beta'}(t) d^*_{\alpha' \beta'}(Q, t)}{\frac{P}{M} \cdot d^*_{\alpha \beta}(Q, t)} \frac{\partial}{\partial P} \right), \quad (14.42)$$

with $\Delta E_{\alpha\beta}(t) = E_\alpha(Q, t) - E_\beta(Q, t)$ and $d_{\alpha\beta}(Q, t) = \langle \alpha; Q, t | \partial/\partial Q | \beta; Q, t \rangle$ is the nonadiabatic coupling vector between the time-dependent states $\alpha$ and $\beta$.

To arrive at an algorithm for computing $\chi_{\alpha\alpha'}(t)$, one starts by discretizing the time to obtain

$$\chi_{\alpha\alpha'}(t) = \sum_{\beta\beta'} \mathcal{T} \left\{ \exp \left[ i \sum_n \tau_n \mathcal{L}^t(\tau_n) \right] \right\}_{\alpha\alpha', \beta\beta'} \chi_{\beta\beta'}(t_0), \quad (14.43)$$

where $\sum_n \tau_n = t - t_0$. As in the derivation of the SSTP algorithm [47], one then assumes very small time steps $\tau_n$ and applies the Dyson identity to obtain

$$\chi_{\alpha\alpha'}(t) = \sum_{\beta\beta'} \mathcal{T} \prod_n \left\{ \exp \left[ i \tau_n \tilde{\mathcal{L}}^0_{\alpha\alpha'}(\tau_n) \right] \right.$$

$$\left. \times \left( 1 + \tau_n \tilde{\mathcal{K}}_{\alpha\alpha', \beta\beta'} + \tau_n \mathcal{K}^t_{\alpha\alpha', \beta\beta'} \right) \right\} \chi_{\beta\beta'}(t_0). \quad (14.44)$$

In what follows, it will be assumed that the subsystem-bath coupling is sufficiently weak that the action of $\tilde{\mathcal{K}}_{\alpha\alpha', \beta\beta'}$ can be disregarded. Thus, if $\tau_n = \tau$ for every $n$, then one obtains

$$\chi_{\alpha\alpha'}(t) = \sum_{\beta\beta'} \mathcal{T} \prod_n \left\{ \exp \left[ i \tau \tilde{\mathcal{L}}^0_{\alpha\alpha'}(\tau) \right] \left( 1 + \tau \mathcal{K}^t_{\alpha\alpha', \beta\beta'} \right) \right\} \chi_{\beta\beta'}(t_0). \quad (14.45)$$

In practice, Eq. (14.45) can be evaluated using an analogous procedure to that described in Sect. 14.2.3. At the beginning of each time step, one propagates the phase space point deterministically using $i\tilde{\mathcal{L}}^0_{\alpha\alpha', \beta\beta'}(t)$. Then, at the end of the step, one samples stochastically the nonadiabatic transition due to the driving field. This is done by first sampling with probability $1/2$ one of the two terms of $\mathcal{K}^t_{\alpha\alpha', \beta\beta'}$ in Eq. (14.38). The probability of accepting the transition is defined as

$$\mathcal{P}_{\beta \to \alpha} = \frac{\tau |\langle \dot{\alpha} | \beta \rangle|}{1 + \tau |\langle \dot{\alpha} | \beta \rangle|}, \quad (14.46)$$

while the probability of rejecting the transition is given by

$$\mathcal{Q}_{\beta \to \alpha} = \frac{1}{1 + \tau |\langle \dot{\alpha} | \beta \rangle|}. \quad (14.47)$$

As described in Sect. 14.2.3, the observable is then multiplied by the appropriate MC weight, depending on whether or not the transition is accepted. Finally, the

**Fig. 14.9** Plot of the
time-dependent coherence,
$\langle \sigma_x(t) \rangle$, for the weak
subsystem-field case
$(g = 0.1)$
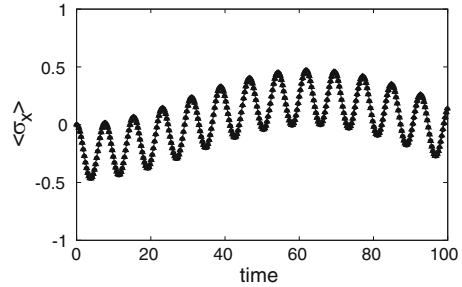


**Fig. 14.10** Plot of the
time-dependent coherence,
$\langle \sigma_x(t) \rangle$, for the strong
subsystem-field coupling case
$(g = 1.5)$
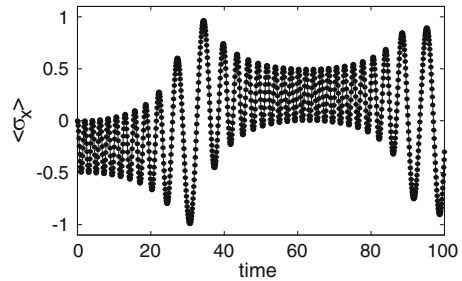


average value of the observable is calculated according to Eq. (14.15), with the use
of the time-dependent basis as opposed to the time-independent one.

The results of the simulations are now presented and discussed. A time step of
$\tau = 0.1$ and $10^5$ trajectories were used to obtain all the results. First, the influence
of the driving field on the metamolecule is investigated by varying the subsystem-
field coupling from $g = 0.1$ to $g = 1.5$ while keeping the system parameters
fixed at $\beta = 12.5$, $c = 0.01$, $\Omega = 0.8$, $\omega = 0.5$ and $\omega_d = 0.05$. For this set
of parameter values, the coupling between the quantum dot and resonant mode is
weak, and, therefore, the effect of nonadiabatic transitions (due to this coupling)
on the dynamics is expected to be minor. Figure 14.9 shows the results for the
time-dependent subsystem coherence, $\langle \sigma_x(t) \rangle$, in the $g = 0.1$ case. We see that
$\langle \sigma_x(t) \rangle$ exhibits both high- and low-frequency oscillatory modes, with the values
of $\langle \sigma_x(t) \rangle$ ranging between $-0.5$ and $0.5$. The fast mode (with angular frequency
$\approx 0.81$) is superimposed on the slow mode (with angular frequency $\approx 0.05$). The
low frequency corresponds to that of the driving field, while the high frequency
corresponds to that of the tunnel splitting, shifted by a very small amount due to the
weak coupling to the bath and field. As expected, in the case of weak coupling to
the driving field, the tunnel splitting dominates the time evolution of $\langle \sigma_x(t) \rangle$.

Figure 14.10 shows the results for the time-dependent subsystem coherence,
$\langle \sigma_x(t) \rangle$, in the $g = 1.5$ case. When strongly coupled to the driving field, the time
evolution of $\langle \sigma_x(t) \rangle$ displays an irregular pattern, viz. it starts by rapidly oscillating
around $\langle \sigma_x \rangle = -0.25$ between $t = 0$ and $t \approx 20$; it undergoes large oscillations
from $t \approx 20$ to $t \approx 40$ and then switches to oscillating rapidly around $\langle \sigma_x \rangle = 0.25$
until $t = 80$; and finally, it undergoes large oscillations again. Based on these

Fig. 14.11 Plot of the time-dependent population difference, $\langle \sigma_z(t) \rangle$, for the strong subsystem-field coupling case ($g = 1.5$)
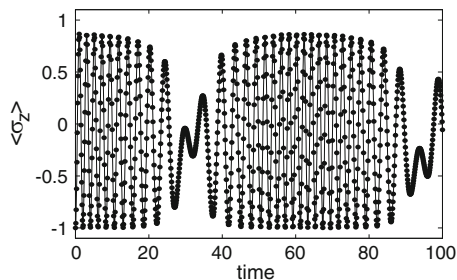


Fig. 14.12 Rate of change of the expectation value of the Hamiltonian of the metamolecule, $d\langle H_M \rangle / dt$, as a function of time. The main figure displays the result for the strong driving field case, while the inset shows the result for the weak driving field case
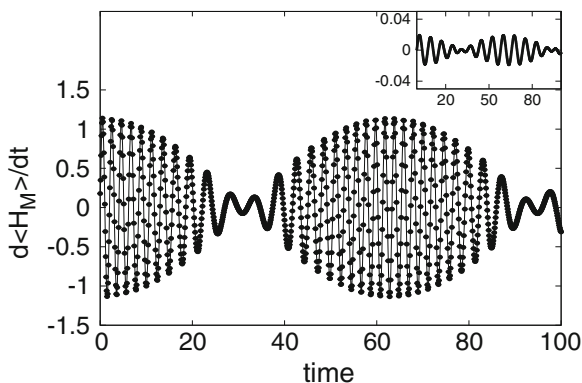


results, one can conclude that the quantum dot switches between two different dynamical regimes, one in which the coherence is positive and the other in which it is negative. Because of the strong coupling to the driving field, the frequency of the fast oscillations is $\approx 200\%$ greater than that obtained in the weak subsystem-field coupling case.

Figure 14.11 shows the time evolution of the subsystem population difference, $\langle \sigma_z(t) \rangle$, in the strong driving regime. It also exhibits an irregular pattern, with regions of large and fast oscillations separated by regions of small and slow oscillations. In the weak driving regime, such a behaviour is not observed, and the amplitude of the oscillations is much smaller (result not shown). This is simply a reflection of the fact that a smaller fraction of the trajectories is driven into the excited state by the driving field in this regime.

Figure 14.12 shows the rate of change of the expectation value of the energy of the metamolecule for the $g = 0.1$ and $g = 1.5$ cases. For $g = 1.5$, we see that $d\langle H_M(t) \rangle / dt$ exhibits regions of large and fast oscillations about zero separated by regions of small and slow oscillations about zero, in the same time intervals where $\langle \sigma_x(t) \rangle$ and $\langle \sigma_z(t) \rangle$ do. Instead, for $g = 0.1$, $d\langle H_M(t) \rangle / dt$ exhibits much smaller oscillations about zero.

## 14.4    Summary and Future Outlook

Quantum dynamical modelling of nanoscale systems containing large numbers of DOF is essential for understanding their microscopic and macroscopic properties. Adiabatic mixed quantum-classical dynamics simulations, which rely on the Born-Oppenheimer approximation, may be performed when there is a large separation between the timescales of the quantum subsystem and classical environment. However, for many chemical and biological processes of interest, this is not the case, and, as a result, the dynamics is not confined to a single state of the quantum subsystem. This has prompted the development of mixed quantum-classical methods for simulating nonadiabatic dynamics.

   In this chapter, we discussed a hybrid MD/MC method known as the SSTP algorithm, which is based on a solution of the QCLE. This method has been shown to perform quite well on relatively simple model systems, but its extension to systems containing multiple (i.e. >2) quantum DOF and strong subsystem-bath coupling has proven to be challenging. This is primarily due to the rapid growth of MC weights (associated with the stochastic sampling of the nonadiabatic transitions) in time, which render the expectation values difficult to converge. To alleviate this problem, observable cutting and transition filtering techniques have been put forward, which significantly reduce the number of trajectories required for convergence of the expectation values. In this chapter, we discussed one transition filtering scheme, which is designed to filter out the low-probability transitions (which lead to the large MC weights) and thereby slow down the growth of the weights. This scheme has been shown to yield substantial improvements in accuracy, as compared to the other schemes, and to generate results with at least one order of magnitude fewer trajectories than what would be required without the scheme. We also discussed a simple procedure for ensuring sign continuity/consistency in the evolution of eigenvectors within an ensemble of surface-hopping trajectories. This is required because the on-the-fly numerical diagonalization of the Hamiltonian matrix can yield eigenvectors with arbitrary signs. Without such a scheme, trajectory-based calculations of expectation values in the adiabatic representation can be adversely affected.

   This chapter also covered two recent applications of the SSTP algorithm. The first one demonstrated the efficacy of the aforementioned transition filtering scheme for simulating vibrational energy transfer dynamics in systems with higher dimensional Hilbert spaces and phase spaces. In particular, the time-dependent populations of the amide I modes in a model of an alpha-helical polypeptide (containing six quantum and six classical coordinates) were presented. The results showed that it is possible to obtain smooth, reliable profiles with more than one order of magnitude fewer trajectories compared to those obtained without any filtering. In the second application, we presented a dynamical study of a model for a plasmonic metamolecule interacting with an oscillatory driving field. In this case, the Hamiltonian is explicitly time-dependent, and, thus, the SSTP algorithm had to be generalized to account for this fact. Results showing the effects of the

driving strength on the population and coherence dynamics of the quantum dot, as well as on the rate of change of the metamolecule energy, were presented and discussed. Interestingly, in the strong subsystem-field coupling case, large and irregular variations in the populations and coherences of the quantum dot were observed.

The QCLE-based approach to modelling quantum dynamics in classical environments has proven to be successful in studying a variety of quantum processes at the nanoscale. Nevertheless, the currently available algorithms present significant challenges, necessitating the need for further improvements and developments. Thus, we hope that this chapter will stimulate research along this direction. In addition, we are interested in broadening the scope of applications studied by the methods discussed herein. In particular, we believe that these methods can be effectively used to study energy and charge transfer dynamics in nanoscale devices.

## Appendix

The following adimensional coordinates and parameters were used to express the metamolecule Hamiltonian in Eq. (14.33):

$$\Omega = \frac{\Omega'}{\omega'_a} \, , \tag{14.48}$$

$$P = \frac{P'}{\sqrt{M'\hbar\omega'_a}} \, , \tag{14.49}$$

$$Q = \sqrt{\frac{\hbar\omega'_a}{\hbar}} Q' \, , \tag{14.50}$$

$$\omega = \frac{\omega'}{\omega'_a} \, , \tag{14.51}$$

$$c = \frac{c'}{\sqrt{\hbar\omega'^3_a M'}} \, , \tag{14.52}$$

$$g = \frac{g'}{\hbar\omega'_a} \, , \tag{14.53}$$

$$\beta = \hbar\omega'_a \beta' \, , \tag{14.54}$$

where the primed quantities denote coordinates and parameters with dimensions and $M'$ is the inertial parameter of the resonant mode (which has been set to unity). In the above equations, the energy scale $\hbar\omega'_a$ has been introduced. $\omega'_a$ is chosen in such a way that the frequency $\omega = 0.5$ of the resonant mode corresponds to $\omega' = 8.9 \times 10^{12}$ Hz (which is typical of metal nanoparticles [51]) and a total simulation time of $5.62 \times 10^{-12}$ s.

# References

1. F. Agostini, S.K. Min, A. Abedi, E.K.U. Gross, J. Chem. Theory Comput. **12**, 2127 (2016)
2. I.V. Aleksandrov, Z. Naturforsch. A **36**, 902 (1981)
3. S.M. Bai, W.W. Xie, Q. Shi, J. Phys. Chem. A **118**, 9262 (2014)
4. A. Bastida, C. Cruz, J. Zúñiga, A. Requena, B. Miguel, The Ehrenfest method with quantum corrections to simulate the relaxation of molecules in solution: equilibrium and dynamics. J. Chem. Phys. **126**(1), 014503 (2007)
5. M.J. Bedard-Hearn, R.E. Larsen, B.J. Schwartz, J. Chem. Phys. **123**, 234106 (2005)
6. E.R. Bittner, P.J. Rossky, Quantum decoherence in mixed quantum-classical systems: nonadiabatic processes. J. Chem. Phys. **103**, 8130–8143 (1995)
7. E.R. Bittner, B.J. Schwartz, P.J. Rossky, Quantum decoherence: a consistent histories treatment of condensed phase non-adiabatic quantum molecular dynamics. J. Mol. Struct. Theochem **389**, 203–216 (1997)
8. S. Bose, Quantum communication through an unmodulated spin chain. Phys. Rev. Lett. **91**(20), 207901 (2003)
9. J.G. Bouillard, W. Dickson, D.P. O'Connor, G.A. Wurtz, A.V. Zayats, Low-temperature plasmonics of metallic nanostructures. Nano Lett. **12**, 1561 (2012)
10. C. Brooksby, O.V. Prezhdo, Quantized mean-field approximation. Chem. Phys. Lett. **346**, 463–469 (2001)
11. X. Chen, S. Li, C. Xue, M.J. Banholzer, G.C. Schatz, C.A. Mirkin, Plasmonic focusing in rod-sheath heteronanostructures. ACS Nano **3**, 87 (2009)
12. D. Dell'Angelo, G. Hanna, Self-consistent filtering scheme for efficient calculations of observables via the mixed quantum-classical liouville approach. J. Chem. Theory Comput. **12**, 477–485 (2016)
13. D. Dell'Angelo, G. Hanna, Using multi-state transition filtering to improve the accuracy of expectation values via mixed quantum-classical Liouville dynamics. AIP Conf. Proc. **1790**, 020009(1)–020009(4) (2016)
14. D. Dell'Angelo, G. Hanna, Importance of eigenvector sign consistency in computations of expectation values via mixed quantum-classical surface-hopping dynamics. Theor. Chem. Acc. **136**, 75 (2017)
15. D. Dell'Angelo, G. Hanna, On the performance of multi-state transition filtering in mixed quantum-classical Liouville surface-hopping simulations: beyond two- and three-state quantum subsystems. Theor. Chem. Acc. **137**, 15 (2018)
16. A. Donoso, D. Kohen, C.C. Martens, Simulation of nonadiabatic wave packet interferometry using classical trajectories. J. Chem. Phys. **112**, 7345 (2000)
17. A. Donoso, C.C. Martens, Simulation of coherent nonadiabatic dynamics using classical trajectories. J. Phys. Chem. A **102**, 4291–4300 (1998)
18. A. Donoso, C.C. Martens, Semiclassical multistate Liouville dynamics in the adiabatic representation. J. Chem. Phys. **112**, 3980 (2000)
19. L.F. Errea, L. Fernández, A. Macías, L. Méndez, I. Rabadán, A. Riera, Sign-consistent dynamical couplings between ab initio three-center wave functions. J. Chem. Phys. **121**(4), 1663–1669 (2004)
20. S.A. Fischer, C.T. Chapman, X. Li, J. Chem. Phys. **135**, 144102 (2011)
21. H. Freedman, G. Hanna, Mixed quantum-classical Liouville simulation of vibrational energy transfer in a model alpha-helix at 300 K. Chem. Phys. **477**, 74–87 (2016)
22. V.I. Gerasimenko, Theor. Math. Phys. **50**, 77 (1982)
23. G. Hanna, R. Kapral, Quantum-classical Liouville dynamics of nonadiabatic proton transfer. J. Chem. Phys. **122**, 244505 (2005)
24. G.J. Hedley, A. Ruseckas, I.D. Samuel, Light harvesting for organic photovoltaics. Chem. Rev. **117**(2), 796–837 (2016)
25. I. Horenko, C. Salzmann, B. Schmidt, C. Schütte, J. Chem. Phys. **117**, 11075 (2002)

26. I. Horenko, C. Salzmann, B. Schmidt, C. Schütte, Quantum-classical Liouville approach to molecular dynamics: surface hopping Gaussian phase-space packets. J. Chem. Phys. **117**, 11075–11088 (2002)
27. C.Y. Hsieh, R. Kapral, J. Chem. Phys. **137**, 22A507 (2012)
28. C.Y. Hsieh, R. Kapral, Analysis of the forward-backward trajectory solution for the mixed quantum-classical Liouville equation. J. Chem. Phys. **138**(13), 134110 (2013)
29. A.W. Jasper, C. Zhu, S. Nangia, D.G. Truhlar, Faraday Discuss. **127**, 1 (2004)
30. C. Joachim, M.A. Ratner, Molecular electronics: some views on transport junctions and beyond. Proc. Natl. Acad. Sci. U. S. A **102**(25), 8801–8808 (2005)
31. R. Kapral, J. Phys. Condens. Matter. **27**, 073201 (2015)
32. R. Kapral, Chem. Phys. **481**, 77 (2016)
33. R. Kapral, G. Ciccotti, J. Chem. Phys. **110**, 8919–8929 (1999)
34. R. Kapral, G. Ciccotti, Mixed quantum-classical dynamics. J. Chem. Phys. **110**, 8919–8929 (1999)
35. A. Kelly, T.E. Markland, J. Chem. Phys. **139**, 014104 (2013)
36. A. Kelly, T.E. Markland, Efficient and accurate surface hopping for long time nonadiabatic quantum dynamics. J. Chem. Phys. **139**(1), 014104 (2013)
37. A. Kelly, R. van Zon, J.M. Schofield, R. Kapral, J. Chem. Phys. **136**, 084101 (2012)
38. K.L. Kelly, E. Coronado, L.L. Zhao, G.C. Schatz, The optical properties of metal nanoparticles: the influence of size, shape, and dielectric environment. J. Phys. Chem. B **107**, 668 (2003)
39. H. Kim, R. Kapral, Chem. Phys. Chem. **9**, 470 (2008)
40. H. Kim, A. Nassimi, R. Kapral, J. Chem. Phys. **129**, 084102 (2008)
41. H.W. Kim, Y.M. Rhee, J. Chem. Phys. **140**, 184106 (2014)
42. S. Lal, S. Link, N.J. Halas, Nano-optics from sensing to waveguiding. Nat. Photon. **1**, 641 (2007)
43. Z. Lin, I.V. Rubtsov, Constant-speed vibrational signaling along polyethyleneglycol chain up to 60-Å distance. Proc. Natl. Acad. Sci. U. S. A. **109**(5), 1413–1418 (2012)
44. J. Liu, G. Hanna, J. Phys. Chem. Lett. **9**, 3928 (2018)
45. D. MacKernan, G. Ciccotti, R. Kapral, J. Chem. Phys. **116**, 2346–2353 (2002)
46. D. MacKernan, G. Ciccotti, R. Kapral, Trotter-based simulation of quantum-classical dynamics. J. Phys. Chem. B **112**, 424 (2008)
47. D. MacKernan, R. Kapral, G. Ciccotti, Sequential short-time propagation of quantum-classical dynamics. J. Phys. Condens. Matter. **14**, 9069–9076 (2002)
48. C.C. Martens, J. Phys. Chem. Lett. **7**, 2610 (2016)
49. C.C. Martens, J. Fang, Semiclassical-limit molecular dynamics on multiple electronic surfaces. J. Chem. Phys. **106**, 4918 (1997)
50. C.C. Martens, J.Y. Fang, J. Chem. Phys. **106**, 4918 (1997)
51. K.R. McEnery, M.S. Tame, S.A. Maier, M.S. Kim, Tunable negative permeability in a quantum plasmonic metamaterial. Phys. Rev. A **89**, 013822 (2014)
52. C.L. Nehl, J.H. Hafner, Shape-dependent plasmon resonances of gold nanoparticles. J. Mater. Chem. **18**, 2415 (2008)
53. S. Nielsen, R. Kapral, G. Ciccotti, Non-adiabatic dynamics in mixed quantum-classical systems. J. Stat. Phys. **101**, 225–242 (2000)
54. A. Nitzan, M.A. Ratner, Electron transport in molecular wire junctions. Science **300**(5624), 1384–1389 (2003)
55. P.V. Parandekar, J.C. Tully, Detailed balance in Ehrenfest mixed quantum-classical dynamics. J. Chem. Theory Comput. **2**(2), 229–235 (2006)
56. M. Pelton, J. Aizpurua, G. Bryant, Metal-nanoparticle plasmonics. Laser Photon. Rev. **2**, 136 (2008)
57. V. Pouthier, Energy transfer in finite-size exciton-phonon systems: confinement-enhanced quantum decoherence. J. Chem. Phys. **137**(11), 114702 (2012)
58. V. Pouthier, Vibrational exciton mediated quantum state transfer: simple model. Phys. Rev. B **85**(21), 214303 (2012)

59. V. Pouthier, Vibrons in finite size molecular lattices: a route for high-fidelity quantum state transfer at room temperature. J. Phys. Condens. Matter. **24**(44), 445401 (2012)
60. O.V. Prezhdo, Mean field approximation for the stochastic Schrödinger equation. J. Chem. Phys. **111**, 8366–8377 (1999)
61. O.V. Prezhdo, V.V. Kisil, Phys. Rev. A **56**, 162 (1997)
62. M. Ratner, A brief history of molecular electronics. Nat. Nanotechnol. **8**(6), 378 (2013)
63. M. Santer, U. Manthe, G. Stock, Quantum-classical Liouville description of multi-dimensional nonadiabatic molecular dynamics. J. Chem. Phys. **114**, 2001 (2001)
64. J.R. Schmidt, P.V. Parandekar, J.C. Tully, Mixed quantum-classical equilibrium: surface hopping. J. Chem. Phys. **129**(4), 044104 (2008)
65. A. Sergi, D. MacKernan, G. Ciccotti, R. Kapral, Simulating quantum dynamics in classical environments. Theor. Chem. Acc. **110**, 49–58 (2003)
66. A. Sergi, F. Petruccione, Phys. Rev. E **81**, 032101 (2010)
67. N. Shenvi, J.E. Subotnik, W. Yang, Phase-corrected surface hopping: Correcting the phase evolution of the electronic wavefunction. J. Chem. Phys. **135**(2), 024101 (2011)
68. N. Shenvi, J.E. Subotnik, W. Yang, Simultaneous-trajectory surface hopping: a parameter-free algorithm for implementing decoherence in nonadiabatic dynamics. J. Chem. Phys. **134**(14), 144102 (2011)
69. J.E. Subotnik, Augmented Ehrenfest dynamics yields a rate for surface hopping. J. Chem. Phys. **132**(13), 134112 (2010)
70. J.E. Subotnik, A. Jain, B. Landry, A. Petit, W. Ouyang, N. Bellonzi, Annu. Rev. Phys. Chem. **67**, 387 (2016)
71. J.E. Subotnik, N. Shenvi, A new approach to decoherence and momentum rescaling in the surface hopping algorithm. J. Chem. Phys. **134**(2), 024105 (2011)
72. M.F. Tame, K.R. McEnery, S.K. Özdemir, J. Lee, S.A. Maier, M.S. Kim, Quantum plasmonics. Nat. Phys. **9**, 329 (2013)
73. D.V. Tsivlin, V. May, Multidimensional wave packet dynamics in polypeptides: coupled amide-exciton chain-vibrational motion in an $\alpha$-helix. Chem. Phys. **338**(2–3), 150–159 (2007)
74. J.C. Tully, J. Chem. Phys. **93**, 1061–1071 (1990)
75. J.C. Tully, Molecular dynamics with electronic transitions. J. Chem. Phys. **93**, 1061 (1990)
76. J.C. Tully, Faraday Discuss. **110**, 407–419 (1998)
77. J.C. Tully, Nonadiabatic dynamics, in *Modern Methods for Multidimensional Dynamics Computations in Chemistry*, ed. by D.L. Thompson (World Scientific, New York, 1998), p. 34
78. D.A. Uken, A. Sergi, Quantum dynamics of a plasmonic metamolecule with a time-dependent driving. Theor. Chem. Acc. **134**, 141 (2015)
79. D.A. Uken, A. Sergi, F. Petruccione, Phys. Scr. **T143**, 014024 (2011)
80. D.A. Uken, A. Sergi, F. Petruccione, Filtering schemes in the quantum-classical Liouville approach to nonadiabatic dynamics. Phys. Rev. E **88**, 033301 (2013)
81. C. Wan, J. Schofield, J. Chem. Phys. **113**, 7047 (2000)
82. C. Wan, J. Schofield, Exact and asymptotic solutions of the mixed quantum-classical Liouville equation. J. Chem. Phys. **112**, 4447 (2000)
83. C. Wan, J. Schofield, Mixed quantum-classical molecular dynamics: aspects of multithreads algorithms. J. Chem. Phys. **113**, 7047 (2000)
84. L.J. Wang, A. Akimov, O.V. Prezhdo, J. Phys. Chem. Lett. **7**, 2100–2112 (2016)
85. L.J. Wang, A.E. Sifain, O.V. Prezhdo, J. Phys. Chem. Lett. **6**, 3827–3833 (2015)
86. F. Webster, E.T. Wang, P.J. Rossky, R.A. Friesner, Stationary-phase surface hopping for nonadiabatic dynamics – two-state systems. J. Chem. Phys. **100**, 4835–4847 (1994)
87. E. Wigner, Phys. Rev. **40**, 749 (1932)
88. R.P. Xu, Y.Q. Li, J.X. Tang, Recent advances in flexible organic light-emitting diodes. J. Mater. Chem. C **4**(39), 9116–9142 (2016)
89. W.Y. Zhang, R. Balescu, J. Plasma Phys. **40**, 199 (1988)
90. J. Zuloaga, E. Prodan, P. Nordlander, Quantum plasmonics: nonlinear effects in the field enhancement of a plasmonic nanoparticle dimer. ACS Nano **4**, 5269 (2010)